Springer

KSME

Journal of Mechanical Science and Technology 33 (1) (2019) 95~108
www.springerlink.com/content/1738-494x(Print)/1976-3824(Online)
DOI 10.1007/s12206-018-1210-9

Diagnosing axle box bearings' fault using a refined phase difference correction method †

Qing Xiong[1,2,3], Weihua Zhang[4], Yanhai Xu[1,2,3,*], Yiqiang Peng[1,2,3] and Pengyi Deng[3]

[1]*Key Laboratory of Fluid and Power Machinery, Ministry of Education, Xihua University, Chengdu, Sichuan 610039, China*
[2]*Key Laboratory of Automotive Measurement, Control and Safety, Xihua University, Chengdu, Sichuan 610039, China*
[3]*School of Automobile and Transportation, Xihua University, Chengdu, Sichuan 610039, China*
[4]*State Key Laboratory of Traction Power, Southwest Jiaotong University, Chengdu, Sichuan 610031, China*

(Manuscript Received February 16, 2018; Revised August 1, 2018; Accepted August 27, 2018)

Abstract

The wheelset treads and axle box bearings of railway vehicles often suffer from fatigue failures. Their regular maintenance highly depends on manual off-line inspection with low working efficiency and poor precision for early failure detection. This study proposes a fault diagnosis method by band-pass filtering and by enveloping the accelerations collected from the axle box bearing on the underfloor wheelset lathe to improve the maintenance efficiency. This process is followed by the refined phase difference correction using the four-term third derivative Nuttall-windowed fast Fourier transform (RPNWF) to extract accurate amplitudes of the fault characteristic frequency and its harmonics. The integration scheme, work flow, and application examples of the fault diagnosis system are presented. Simulation analysis and results show that the developed method can achieve effective diagnosis of the fault and fault degree of axle box bearings as well as yield better correction accuracy than the commonly used discrete spectrum correction methods.

Keywords: Axle box bearing; Fault diagnosis; Underfloor wheelset lathe; Refined phase difference correction method; Nuttall-windowed FFT

1. Introduction

A railway vehicle is usually subjected to different operating conditions with variable speeds, payloads, and ambient temperatures, which inevitably lead to wearing, pitting, and even peeling fault of its core components, such as wheel treads and axle box bearings [1-3]. These failures will not only reduce its ride comfort and service life but also impair its safety, which may cause serious economic losses or catastrophic casualties, leading to the emergence of negative social influences [4]. Accidents due to failures of railway vehicles' critical components still occur occasionally [5, 6].

The core components of wheelsets require rigorous and reliable inspections and maintenance to avoid operation accidents [7]. Currently, such inspection and maintenance are conducted separately. On the one hand, an underfloor wheelset lathe (UWL) is usually applied to restore the shape of the worn wheel tread and remove the damage of the wheel tread associated with rolling contact fatigue, wheel flats, and cavities, considering UWL can profile the tread while the wheelset remains in situ on the railway vehicle [8, 9]. On the other hand, although some methods, such as thermal signal analysis [10], acoustic emission [7, 11] and acoustic signal analysis [12], have been occasionally used for continuously and remotely monitoring the axle box bearings, their regular maintenance mainly depend on manual off-line inspection, which suffers from low working efficiency and imprecise fault diagnosis due to heavy weight and small assembly space along with a tedious process comprising several steps [13, 14].

The maintenance period is usually given by the vehicle manufacturer and is related to the type and speed level of the railway vehicles. The typical profile period of wheel treads is approximately 200000 km [15], and the maintenance period of axle box bearings is generally one million km [16]. If the bearings' maintenance and tread repair happen concurrently, the maintenance period and associated cost of the axle box bearings can be reduced. When the UWL is applied, the wheel rotates at a low speed, which provides practically viable conditions for bearing fault diagnosis by monitoring its vibration signals. This method can reduce the manual intervention, which in turn, can improve the diagnostic accuracy and efficiency. To ensure the profiling quality, the profiling speed of UWL must be between 30 and 120 m/min [17] when the wheel tread is repairing. For the standard wheel diameter of 0.84 m [18], the corresponding wheel speed can be calculated as approximately 12 to 46 r/min. At such a low speed, the bearing faults are difficult to identify stably and efficiently.

The current study proposes an applicable method of integrating a fault diagnosis system for axle box bearings based on

*Corresponding author. Tel.: +86 13551024100, Fax.: +86 2887726698
E-mail address: xu_yanhai@163.com
† Recommended by Associate Editor Gyuhae Park
© KSME & Springer 2019

the collected vibration signal with UWL. Without changing the original structure and function of the UWL, this method can effectively diagnose the common faults of the axle box bearings, and is significant in improving and enriching the existing vehicle maintenance strategy.

Practically, the discrete spectrum analysis is the most common method for the fault diagnosis of the rolling bearing. However, this method also has its drawbacks. First, at low-speed condition, the bearing's fault characteristic frequencies and the fault impact energy are insignificant and can easily be disturbed by environmental noise [19]. Second, the discrete spectrum analysis can only act on a limited interval because the computer can only analyze limited samples, which inevitably causes energy leakage due to the truncation in time domain [20]. These drawbacks lead to an error that cannot be ignored in the extraction of amplitude, frequency, and phase of the discrete spectrum; therefore, we cannot directly obtain a quantitative and accurate diagnosis of the fault degrees of rolling bearing by discrete spectrum.

In view of these problems, a refined phase difference correction (RPDC) with the four-term third derivative Nuttall-windowed fast Fourier transform (FFT, RPNWF) method is proposed in this study. This correction method can be potentially applied to realize the quantitative diagnoses of axle box bearing failure at low speeds.

The rest of this paper is organized as follows. Sec. 2 briefly describes the key steps of the phase difference correction (PDC) method and its refined versions (RPDC and RPNWF). Sec. 3 introduces the integrated scheme and the process of fault diagnosis for the axle box bearings. The simulation analysis in Sec. 4 and the application examples in Sec. 5 are demonstrated to verify the effectiveness of the proposed methods. The conclusions and recommendations for future works are given in Sec. 6.

2. PDC, RPDC and RPNWF methods

2.1 Brief introduction of the PDC method

The PDC method was first developed in 2000 by Ding [21] to overcome the problem of energy leakage in discrete spectrum analysis. Here, we briefly describe the key steps of the PDC method.

Given a harmonic signal, $x(t) = A\cos(2\pi f_0 t + \theta)$, its Fourier transform can be obtained as

$$X(f) = \frac{1}{2}Ae^{-j\theta}\delta(f + f_0) + \frac{1}{2}Ae^{j\theta}\delta(f - f_0), \tag{1}$$

where $f = kf_s / N = k\Delta f$, N is the number of sampling points, fs is the sampling frequency, Δf is the frequency resolution, and $\delta()$ is the Dirac delta function.

The signal $x(t)$ is multiplied by a window function $\omega_T(t)$ with length of T, where $T = (N-1)/f_s$. $\omega_T(t)$ is obtained by moving the length $T/2$ from the symmetric window $\omega(t)$ to the right, that is, the phase changes $e^{-j\cdot\pi fT}$. If $W(f)$ and $W_T(f)$ represent the window function spectrums of $\omega(t)$ and $\omega_T(t)$, respectively, the relationship between them can be expressed as

$$W_T(f) = W(f)e^{-j\pi fT}. \tag{2}$$

According to the convolution theorem, the Fourier transform of the signal after adding a window $x(t)\omega_T(t)$ can be written as

$$X_W(f) = \frac{1}{2}AW(f + f_0)e^{-j[\pi T(f+f_0)+\theta]} + \frac{1}{2}AW(f - f_0)e^{-j[\pi T(f-f_0)-\theta]}. \tag{3}$$

The FFT of N points is taken to $x(t)\omega T(t)$. The frequency resolution Δf cannot be infinitesimal; thus, we assume that $f_0 = (K - \Delta K)\Delta f$, where K is an integer and $\Delta K \in [-0.5 \;\; 0.5]$ is a normalized frequency correction. The peak of the discrete spectrum should appear on the *K-th* spectrum line, and its corresponding phase is given by

$$\varphi_1 = \theta - \pi T(K\Delta f - f_0) = \theta - \pi\Delta K. \tag{4}$$

The center of the window function $\omega_T(t)$ moves the length T to the right. When the phase changes $e^{-j\cdot 2\pi fT}$, the phase of the signal after the FFT of N points can be obtained as

$$\varphi_2 = \theta + \Delta K\pi + 2\pi\Delta K = \theta - (\pi + 2\pi)\Delta K. \tag{5}$$

The phase difference can then be calculated as

$$\Delta\varphi = \varphi_1 - \varphi_2 = -2\pi\Delta K, \tag{6}$$

where the value of $\Delta\varphi$ is between -2π and 2π.

However, the phase is an arctan function, and the range of the main value is $(-\pi, \pi)$. Therefore, a proper adjustment of the phase difference $\Delta\varphi$ is carried out using the equation

$$\Delta\varphi = \begin{cases} \Delta\varphi + 2\pi, & \Delta\varphi < -\pi \\ \Delta\varphi - 2\pi, & \Delta\varphi > \pi \end{cases}. \tag{7}$$

The normalized frequency correction is

$$\Delta K = -\frac{\Delta\varphi}{2\pi}. \tag{8}$$

The coefficient of the *K-th* spectrum line of the peak in the spectrum is assumed to be $X(K) = R_K + jI_K$, and the correction formulas for the amplitude and phase of the signal are respectively given by

$$A = \frac{2|X(K)|}{W(\Delta K)}, \tag{9}$$

$$\theta = \tan^{-1}\left(\frac{I_K}{R_K}\right) + \Delta K\pi \,. \tag{10}$$

From Eq. (9), the amplitude correction is entirely dependent on the window function spectrum *W(f)*. With various windows, the window function spectrum *W(f)* is different, so as the amplitude correction formula. In fact, even for the common window function, its spectral function is complex and can only be approximated in numerical calculation. Moreover, the analytical expressions of the spectral functions of some complex window functions are difficult to obtain. This problem greatly restricts the selection flexibility of window function in different applications. Thus, the amplitude correction must be improved accordingly.

2.2 RPDC method

Hu [22] proposed an RPDC method in 2012 to improve the accuracy of amplitude correction. The key steps of the method are described below.

Given a discrete time series with N data points, $x(n)=\{x(0), x(1), ..., x(N-1)\}$, the signal and sampling frequencies are f_0 and f_s, respectively. The inverse transform expression of its discrete Fourier transform can be obtained using the equation

$$x(n) = \sum_{k=0}^{N-1} X(k) e^{j\frac{2\pi}{N}nk} \,, \tag{11}$$

$$e_k = e^{j(2\pi/N)nk} \,,$$

where $n = 0,1,...,N-1,\ k = 0,1,...,N-1$, is assumed. We can then consider the sequence $x(n)$ of N points as a vector in the N dimension linear space. Here, $e_0, e_1, ..., e_{N-1}$ can form a group of bases, and $x(n)$ can be regarded as a linear combination of these bases.In addition, $X(0), X(1), ..., X(N-1)$ are the coordinates of $e_0, e_1, ..., e_{N-1}$.

If the signal frequency $f_0 = K(f_s / N)$, e_k represents a complex sine sequence with frequency of f_0. The corresponding coordinate of e_k *X(K)* has a definite physical meaning, which can be used to directly calculate the amplitude and phase of the signal. If the signal frequency $f_0 = (K - \Delta K)(f_s / N)$, the spectrum leakage will occur.

Here, $e_0, e_1, ..., e_{N-1}$ is multiplied by an N point sequence $e^{-j(2\pi/N)n\Delta K}$, and a group of new bases $\tilde{e}_0, \tilde{e}_1, ..., \tilde{e}_{N-1}$ can be obtained as

$$\tilde{e}_K = e^{j\frac{2\pi}{N}nk} e^{-j\frac{2\pi}{N}n\Delta K} = e^{j\frac{2\pi}{N}n(k-\Delta K)} \,. \tag{12}$$

In addition, $\tilde{X}(0), \tilde{X}(1), ..., \tilde{X}(N-1)$ are the coordinates of $\tilde{e}_0, \tilde{e}_1, ..., \tilde{e}_{N-1}$. *x(n)*, which can also be expressed as

$$x(n) = \sum_{k=0}^{N-1} \tilde{X}(k)\tilde{e}_k = e^{-j\frac{2\pi}{N}n\Delta K} \sum_{k=0}^{N-1} \tilde{X}(k) e_k \,, \tag{13}$$

where $\tilde{e}_k$ represents a complex sine sequence with the frequency of $f_0 = (K - \Delta K)(f_s / N)$. The corresponding coordinate of e_k *X(K)* has a definite physical meaning, which can be used to directly calculate the amplitude and phase of the signal. If the signal frequency $f_0 = (K - \Delta K)(f_s / N)$, the spectrum leakage will occur. The amplitude and phase of the signal can be calculated accurately by the coordinate $\tilde{X}(k)$ corresponding to $\tilde{e}_k$, and the leakage will not be produced. However, Eq. (13) cannot be directly calculated by the FFT algorithm.

Both sides of Eq. (13) are multiplied by $e^{j(2\pi/N)n\Delta K}$, and a new sequence $\tilde{x}(n)$ can be obtained

$$\tilde{x}(n) = x(n)e^{j\frac{2\pi}{N}n\Delta K} = \sum_{k=0}^{N-1} \tilde{X}(k) e^{j\frac{2\pi}{N}nk} \,. \tag{14}$$

Eq. (14) is an expression of a standard inverse discrete Fourier transform. The coefficient $\tilde{X}(k)$ in the formula can be calculated by FFT for the N point sequence $\tilde{x}(n)$. Its physical meaning is that when the signal frequency f_0 of the sequence $x(n)$ falls between two spectral lines on the discrete spectrum, the spectrum will leak out. Multiplying $x(n)$ by a sequence $e^{j(2\pi/N)n\Delta K}$ is equivalent to causing a frequency shift of the signal. The signal frequency of the new sequence is only aligned with the *K-th* spectrum line on the discrete frequency spectrum; therefore, no leakage will occur.

The amplitude of the spectrum after adding windows will be reduced by the influence of the window function. Accordingly, we assume that the *K-th* coefficient obtained by FFT on signal after adding windows $\tilde{x}_\omega(n) = \tilde{x}(n)\omega(n)$ is given by

$$\tilde{X}_\omega(K) = \tilde{R}_K + j\tilde{I}_K \,. \tag{15}$$

On the basis of Eqs. (9) and (10) from the analysis in this section, the amplitude and phase correction formulas for the initial signal $x(n)$ can be respectively expressed as

$$A = \frac{2\left|\tilde{X}_\omega(K)\right|}{W(0)} \,, \tag{16}$$

$$\theta = \tan^{-1}\left(\frac{\tilde{I}_K}{\tilde{R}_K}\right) . \tag{17}$$

where $W(0)$ is the direct component of $\omega(n)$. This component only needs the average value of the window function without knowing the expression of the window spectrum function.

2.3 RPNWF method

The RPDC method proposed by Hu et al. [22] improves the amplitude accuracy of the traditional PDC method and achieves good correction results in the simulation test of dense spectrum. The selection of the window function exerts a great impact on this method. However, only the combined effect of the improved method has been investigated with the tradi-

tional window functions, such as rectangular and Hanning windows. To the best of our knowledge, no in-depth study on window functions with superior sidelobe performances has been performed.

On the one hand, the fault signal of the axle box bearing is harmonic with the fault characteristic frequency as the fundamental one. On the other hand, under low-speed condition, the spectrum of the inner-race faults and ball faults of the axle box bearing are dense with various frequency components. A window function with a small sidelobe peak and a large sidelobe falloff rate must be selected to analyze this type of dense harmonic signal.

The four-term third derivative Nuttall window (for convenience, it is referred to as Nuttall43 hereafter) [23] is a combinational cosine window with small leaking; its sidelobe peak and falloff rate are -83 dB and 30 dB/octave, respectively. Unlike the comprehensive performances of the sidelobe of other window functions, Nuttall43's performance is superior, and it has been successfully applied in many fields of harmonic analysis [24-26].

Therefore, this study combines the RPDC method with the Nuttall43-windowed FFT (RPNWF) to explore the effectiveness of quantitative diagnosis of axle box bearings at low speed. Given a discrete time series with N data points, $x(n)=\{x(0),x(1),...,x(N-1)\}$, the detailed process of RPNWF is presented below.

a. Normalized frequency correction ΔK of envelope signal $x(n)$ is achieved by the phase difference method.

b. According to Eq. (14), multiplying $x(n)$ by an N point sequence $e^{j(2\pi/N)n\Delta K}$ generates a new sequence $\tilde{x}(n)$.

c. The signal $\tilde{x}_\omega(n)=\tilde{x}(n)\omega(n)$ is obtained after adding Nuttall43 window, where $\omega(n)$ is as follows:

$$\omega(n)=0.338946-0.481973*\cos(2\pi*n/N)+0.161054*\cos(4\pi*n/N)-0.018027*\cos(6\pi*n/N)$$

d. $\tilde{X}_\omega(K)$ is calculated by the FFT. The correction formula is used to accurately calculate the amplitudes at the fault characteristic frequency and its harmonic components of axle box bearing, which can indicate the existence of the fault and the fault degree.

3. Brief introduction of the integrated scheme

3.1 System workflow

A typical UWL, as illustrated in Fig. 1, is composed of the frame, track system, positioning device, parameter-measuring device, supporting device, clamping device, profiling device, and numerical control system [27]. The system workflow that integrates the bearings' fault diagnosis with UWL is shown in Fig. 2.

The proposed system work flow can be summarized via the following steps:

a. During the interaction of the clamping device, supporting device, and driving friction wheels, the measured wheel is firmly fixed in the center position of UWL.

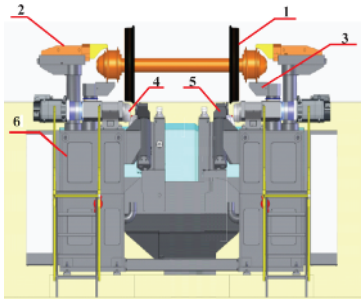

Fig. 1. Underfloor wheelset lathe: (1) Wheelset; (2) clamping device; (3) supporting device; (4) driving friction wheel; (5) profiling device; (6) frame.

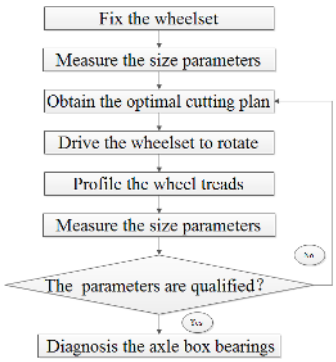

Fig. 2. System workflow.

b. The parameter-measuring device measures the size parameters of the wheel set, such as the wheel diameter, inner distance, flange thickness, and flange height. The numerical control system calculates these parameters to form the optimum profiling scheme.

c. Under the action of the two driving friction wheels, the wheel set begins to rotate and reaches a predetermined speed. The profiling device is raised, and repair starts.

d. After one profiling work, the device measures the relevant parameters again. If the parameters remain unqualified, step (b) is repeated until all parameters are qualified.

e. When all parameters are qualified, the profiling tool is put down. The wheel set continues to rotate and enters the fault diagnosis stage of the axle box bearings.

The bearing fault diagnosis scheme we proposed above is implemented after the completion of the profiling work for two reasons. First, in the profiling process, the profiling tool that comes into contact with the wheel tread will produce additional vibration. Second, when the profiling work is completed, the wheel tread will be smooth; thus, the signal collected by the acceleration sensor has a high signal-to-noise ratio.

3.2 Process of fault diagnosis for the axle box bearings

The fault diagnosis system of the axle box bearings consists of the acceleration sensor, speed sensor, data acquisition de-

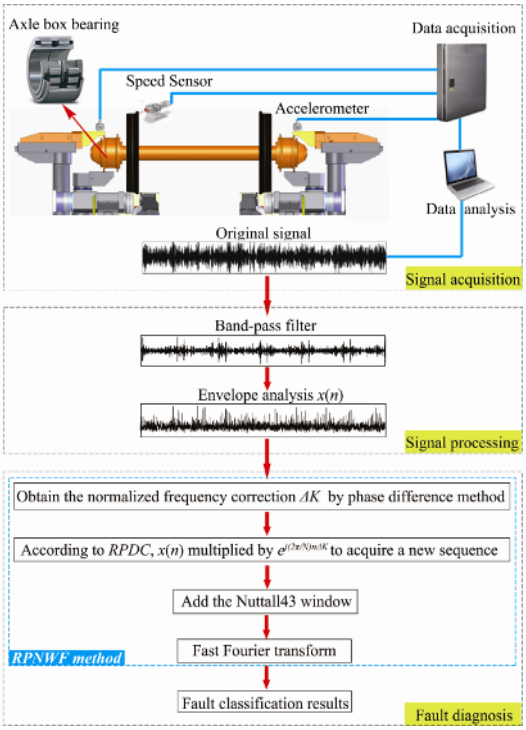

Fig. 3. Process of fault diagnosis for the axle box bearings.

vice, communication lines, and high-performance computer (including analysis software). The specific process of fault diagnosis shown in Fig. 3 can be described below.

a. Data acquisition. The devices are connected as shown in Fig. 3. The two accelerometers are affixed to the left and right clamping devices with two magnetic bases. The speed sensor we selected is a noncontact photoelectric sensor, which we arranged close to the wheel and must face the reflective label on the wheel. The output signals of all sensors are collected and processed by the data acquisition device and then communicated to the high-performance computer through the open platform communications protocol.

b. Signal processing. Band-pass filtering is performed on the original signal obtained by acquisition, after which the envelope analysis is conducted.

c. Fault diagnosis. The RPNWF method is used to accurately calculate the signal amplitude at the fault characteristic frequency and its harmonic components for judging the bearing's fault location and degree.

4. Simulation analysis

The program and simulation are performed in MATLAB platform to verify the application effect of the proposed algorithm.

The rolling bearing's signals with different fault types are assumed to vary in terms of their fault characteristic frequencies, amplitudes, and phases at each harmonic component. In practice, at least three-order harmonics must be identified in the spectrum to determine the bearing fault accurately [28]. Therefore, we adopt the harmonic signal model given by

$$x(t)=\sum_{m=1}^{9}A_m\cos(2\pi\frac{mf_1}{f_s}t+j_m)=\sum_{m=1}^{9}\frac{1}{m}\cos(2\pi\frac{mf_1}{f_s}t+\frac{10m\pi}{180}) . \quad (18)$$

In case of the fundamental frequency f_1 changing from 4.0 Hz to 6.0 Hz with 0.2 Hz as the step length, we use the RPDC (based on Hanning window) algorithm, the RPDC with Blackman-Harris-windowed FFT algorithm (RPBWF), and the RPDC with Nuttall43-windowed FFT algorithm (RPNWF) to calculate the harmonic frequencies, amplitudes, and phases in Eq. (18), respectively. The sampling frequency fs is 320 Hz, and the truncated data length of each windowed FFT is 2048. Fig. 5 shows a comparison of the time and frequency domains, and Table 1 gives the specific sidelobe parameter among the three windows mentioned above [22, 29, 30].

From Table 1, the absolute sidelobe peak value and falloff rate of the Nuttall43 window are obviously higher than those

Table 1. Comparison of the sidelobe performance among the three windows.

Window function	Sidelobe peak (dB)	Sidelobe falloff rate (dB/octave)
Hanning	-31	18
Blackman-Harris	-92	6
Nuttall43	-83	30

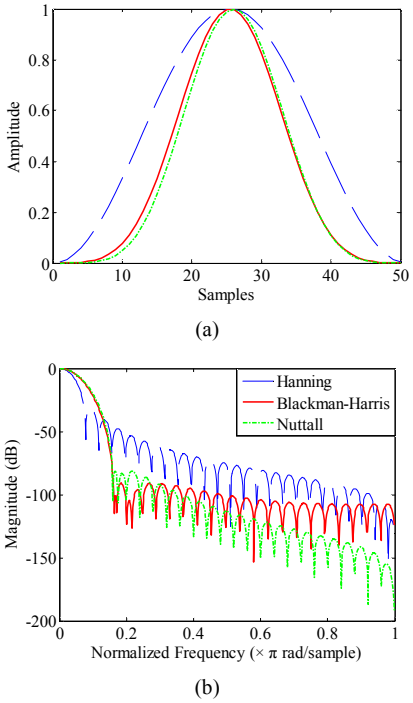

Fig. 4. Comparison of the time and frequency domains among the three windows: (a) Time domain; (b) frequency domain.

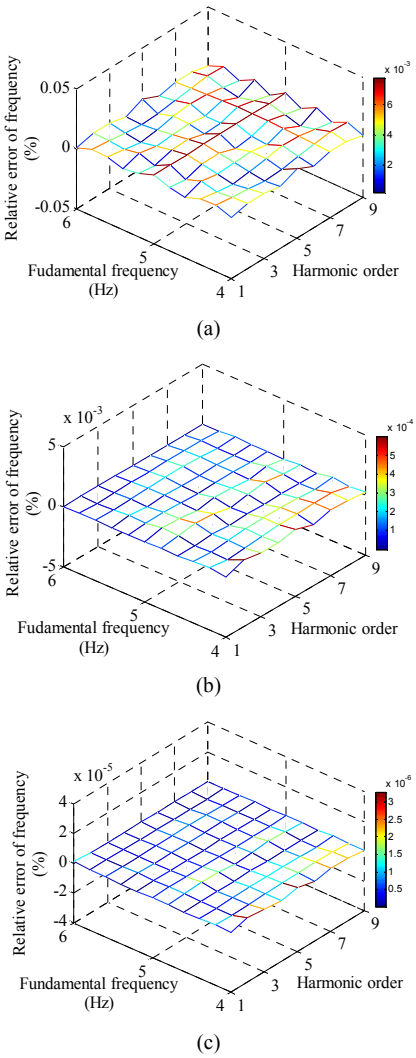

Fig. 5. Relative errors of harmonic frequencies that correspond to the different algorithms: (a) RPDC; (b) RPBWF; (c) RPNWF.

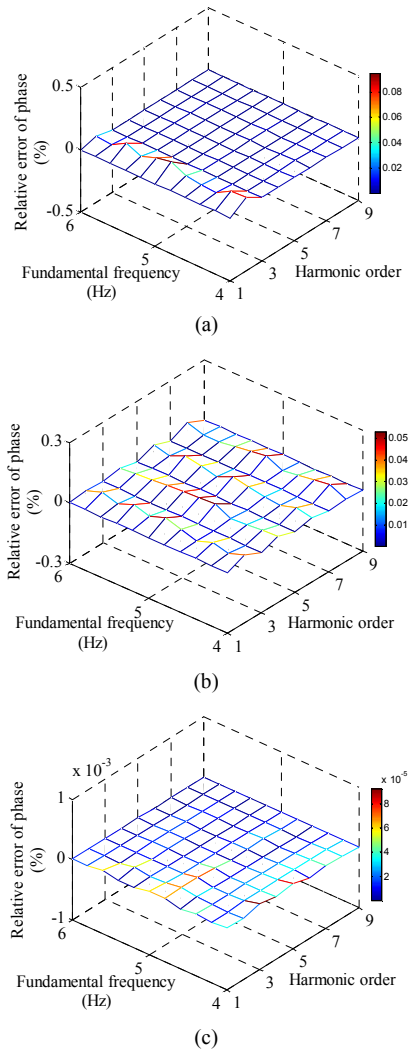

Fig. 6. Relative errors of harmonic phases corresponding to the different algorithms: (a) RPDC; (b) RPBWF; (c) RPNWF.

of the Hanning window. Although the Nuttall43 window's absolute sidelobe peak value is slightly smaller than the Blackman-Harris window, its sidelobe falloff rate is 5 times greater than that of the latter. Therefore, the overall performance of the sidelobe of the Nuttall43 window is the best among the three candidates. Fig. 5 shows the relative errors of harmonic frequencies corresponding to the different algorithms.

The three-color bars illustrated in Fig. 5 indicate that the maximum frequency relative errors of the RPDC, RPBWF and RPNWF algorithms are approximately $8*10^{-3}$, $6*10^{-4}$ and $3*10^{-6}$, respectively. Among the three algorithms, the RPNWF has the highest frequency measurement precision, and in terms of the uniformity of color distribution, the surface formed by all points in the RPNWF is the flattest. Except for a few points with high value (color red or yellow), most of the points in the RPNWF are evenly distributed (the color is blue), indicating that it has the best stability in harmonic frequency measurement. By contrast, the surface formed by all points in the RPDC is rough and uneven, which implies that the stability of the RPDC for the harmonic frequency measurement is the worst among the three methods.

The relative errors of harmonic phases corresponding to the different algorithms are shown in Fig. 6. The maximum phase relative errors of RPDC, RPBWF and RPNWF are approximately 0.1, 0.05 and $9*10^{-5}$, respectively. The accuracy of the RPNWF is obviously better than those of the other two algorithms. Moreover, the surface formed by all points in the RPNWF is the flattest, and the colors are evenly distributed; hence, it has the best stability in harmonic phase measurement of the three algorithms. The maximum relative error of the RPDC is concentrated on the second-order harmonics. The falloff of the first sidelobe in the Hanning window is relatively small, which leads to the second-order harmonics presenting major leakage. Among the the three methods, the falloff of the first sidelobe in the Blackman-Harris window is the largest

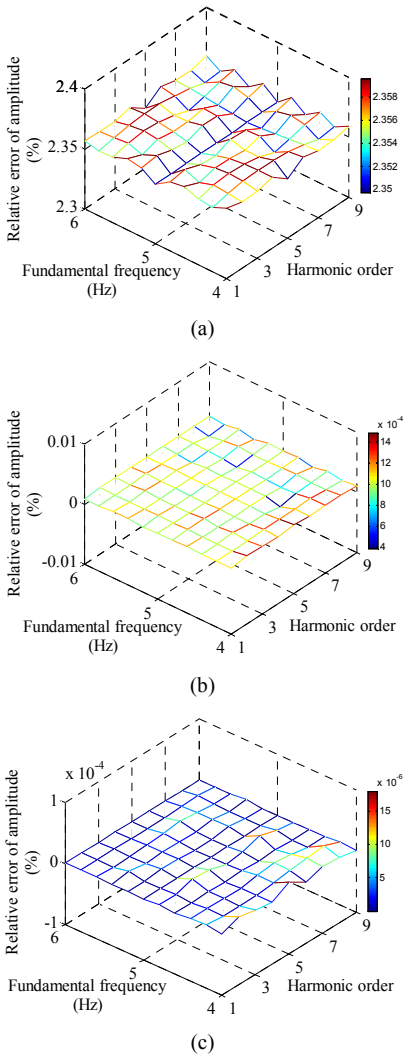

Fig. 7. Relative errors of the harmonic amplitudes corresponding to the different algorithms: (a) RPDC; (b) RPBWF; (c) RPNWF.

(-92 dB), and the falloff speed of its stopband peak is the smallest (6 dB/octave). Thus, there is large error in calculating the even-order harmonic phases of the second, fourth, sixth and eighth orders in the RPBWF.

Fig. 7 shows the relative errors of the harmonic amplitudes corresponding to the different algorithms. The amplitude detection capability of the RPNWF is prominent, the maximum relative error is approximately $1.7*10^{-5}$, and the harmonic amplitude detection accuracy is higher than those of the RPDC (the maximum relative error is approximately 2.36) and the RPBWF (the maximum relative error is approximately $1.5*10^{-3}$). Even for weak- and high-order harmonic components, the RPNWF can also achieve the desired amplitude accuracy.

The above simulation results indicate that the RPNWF not only has more advantages in measuring the accuracy of the three parameters of harmonic frequency, amplitude, and phase, but also has better measurement stability than those of the RPDC with Hanning- and Blackman-Harris-windowed FFT algorithms.

Although the time-domain waveform and sidelobe peak of the Nuttall43 window in Fig. 4 are similar to those of the Blackman-Harris window, the correction accuracy of the harmonic frequency (see Fig. 5), phase (see Fig. 6), and amplitude (see Fig. 7) are 2 or 3 orders of magnitude higher than that of the Blackman-Harris window.

In addition, the correction accuracy of the discrete spectrum is closely related to the sidelobe comprehensive performance of the window function. Either a small sidelobe peak or a large sidelobe falloff rate can lead to unsatisfactory errors. However, the sidelobe falloff rate of the Nuttall43 window (30 dB/octave) is 5 times greater than that of the Blackman-Harris window (6 dB/octave).

Table 2. Geometrical parameters of the bearings.

Axle box bearing	OD (mm)	ID (mm)	PD (mm)	T (mm)	BD (mm)	BT (mm)
NJ(P)3226X1	250	130	190	80	32	52

* OD, ID, PD and T denote the outside diameter, inside diameter, pitch diameter, and bearing thickness, respectively; BD and BT denote the diameter and thickness of ball, respectively.

Table 3. Fault characteristic frequency of the bearings.

Inner-race (Hz)	Outer-race (Hz)	Ball (Hz)	Cage (Hz)
6.1342	4.3658	2.1634	0.3118

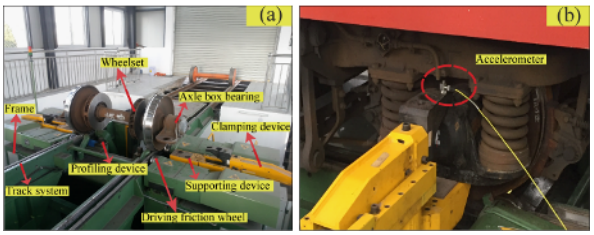

Fig. 8. Experimental setup: (a) UGL-type UWL; (b) installation location of acceleration sensor.

5. Applications

5.1 Data acquisition and processing

We conduct the fault setting test of the axle box bearings on a UGL-type UWL (see Fig. 8(a)) at the Hefei Rolling Stock Depot of the Shanghai Railway Administration. This was carried out with the aim of proving the effectiveness of the method proposed in this study.

The test bearings are double-row cylindrical roller bearings (NJ(P)3226X1), which are widely used in the axle box of the railway vehicles. The geometrical parameters and fault characteristic frequency of the bearings are shown in Tables 2 and 3, respectively.

The Jining Mould Company in Shandong Province provides

Table 4. Fault labels and sizes of seven signals.

Label	Running state	Fault width (mm)	Fault depth (mm)
S1	Normal	0	0
S2	Slight inner-race faults	5	1.5
S3	Serious inner-race faults	10	2.0
S4	Slight outer-race faults	5	1.5
S5	Serious outer-race faults	10	2.0
S6	Slight ball faults	5	1.5
S7	Serious ball faults	10	2.0

Fig. 9. Artificial faults on the components of the axle box bearing: (a) Normal; (b) slight outer-race faults; (c) serious outer-race faults; (d) slight inner-race faults; (e) serious inner-race faults; (f) slight ball faults; (g) serious ball faults.

the test bearings with precise machining to achieve seven faults with different locations and degrees, as shown in Fig. 9. Every fault location consists of two degrees, namely, slight faults (the width is 5 mm, the depth is 1.5 mm) and serious faults (the width is 10 mm, the depth is 2.0 mm).

When the UWL is running, the wheel speed is 45 r/min. In other words, the outer-race of the axle box bearing is fixed, while the inner-race of the axle box bearing rotates with a rotational frequency of 0.75 Hz (the load of the axle box is 80 kN). The accelerometer affixed to the clamping devices of the UWL is instrumented to collect vibration signals (see Fig. 8(b)), with a sampling frequency of 25.6 kHz.

Through the experiments, we obtain seven types of vibration acceleration signals with different fault locations and different fault degrees of axle box bearings. The fault labels and sizes of the seven signals are shown in Table 4.

Fig. 10 illustrates the gathered first half-second acceleration time histories associated with the seven states of axle box

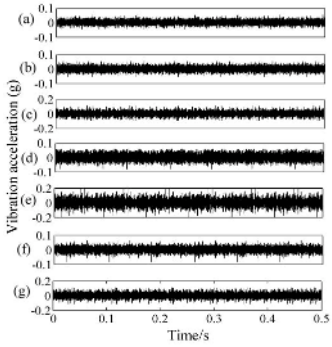

Fig. 10. Original waveforms of the seven vibration acceleration signals: (a) S1; (b) S2; (c) S3; (d) S4; (e) S5; (f) S6; (g) S7.

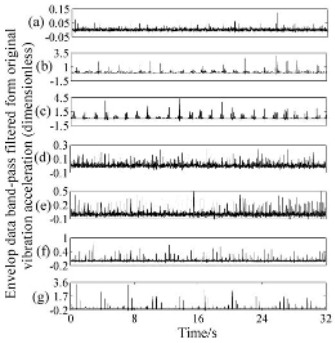

Fig. 11. Waveforms of the seven envelope signals: (a) S1; (b) S2; (c) S3; (d) S4; (e) S5; (f) S6; (g) S7.

bearing. The graph shows that the seven states cannot be distinguished by referring only to the original waveforms.

Band-pass filtering is performed on the original signals to remove the low-frequency noise and enhance the periodic signals containing fault information. According to Ref. [31] and from our repeated experimental experience, we select a 500- to 10-kHz band-pass filter. All the filtered signals are subjected to an envelope detector, and seven types of envelope signals are obtained, as shown in Fig. 11. The amplitude unit of the envelope signal is dimensionless, because the Hilbert transformation is used to demodulate the signal in the envelope analysis [32].

Figs. 10 and 11 indicate that, after band-pass filtering and envelope analysis, the impact characteristics hidden in the signals appear. However, the states of the bearings remain impossible to judge directly through these signals.

5.2 FFT algorithm without correction

We collect the data length of 90 s in each state and divide each data set evenly into 10 segments in order to reduce the randomness of operation.

Envelop analysis is performed on the 10 samples, and we obtain 10 sets of envelop data in each state. All the 70 envelop signals are subjected to the Hanning-windowed FFT algorithm to obtain the FFT spectra. This is a common method in engi-

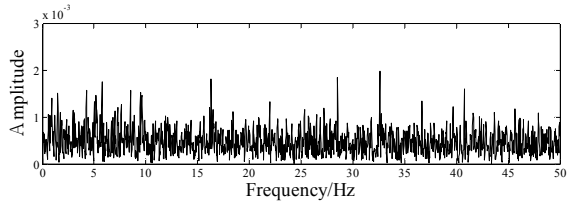

Fig. 12. FFT spectrum of the normal signal.

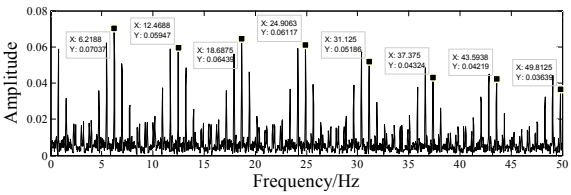

(a)

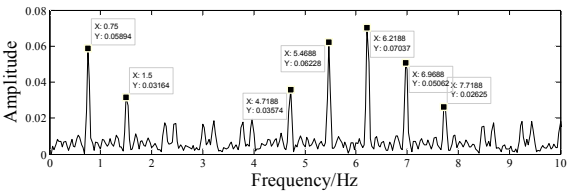

(b)

Fig. 13. FFT spectra of slight inner-race fault signal: (a) 0 to 50 Hz; (b) 0 to 10 Hz.

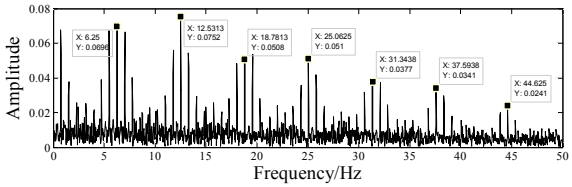

(a)

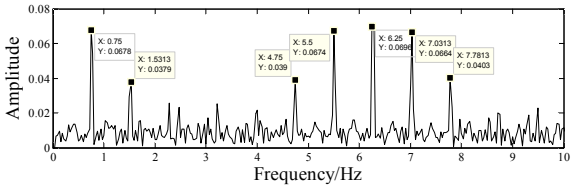

(b)

Fig. 14. FFT spectra of serious inner-race faults signal: (a) 0 to 50 Hz; (b) 0 to 10 Hz.

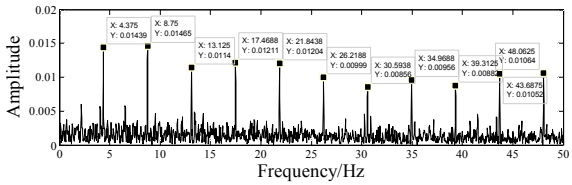

Fig. 15. FFT spectrum of slight outer-race fault signal (0 to 50 Hz).

neering but without correction. Table 3 shows that the maximum failure frequency is 6.1342 Hz; according to the Shannon sampling theorem [33], and from the actual experience, we select the frequency range of 0 to 50 Hz. After averaging, the FFT spectrum of the normal signal is presented in Fig. 12, which shows the irregular distribution of various frequency components.

The FFT spectra of the slight inner-race faults after averaging are illustrated in Figs. 13(a) (0 to 50 Hz) and 14(b) (0 to 10 Hz). In the frequency range of 0 to 50 Hz, spectral peaks occur at the frequency of 6.2188 Hz and its harmonics (12.4688, 18.6875, 24.9063, 31.1250, 37.3750, 43.5938 and 49.8125 Hz). The frequency sidebands of 0.75 Hz are also observed (as shown clearly in Fig. 13(b)) with decreasing amplitudes at both sides of these frequencies. In practice, when the axle box bearing is running, the motions of its balls are not purely rolling, and the rotational speed is imperfectly constant [34]. Thus, the actual fault frequencies are slightly different from the theoretical calculation values in Table 3.

The frequency of 6.2188 Hz is close to the inner-race fault characteristic frequency of 6.1342 Hz, which is calculated in Table 3, and the frequency of 0.75 Hz is the same as the rotational frequency of the inner-race. The vibration amplitude of the inner-race fault characteristic frequency is modulated by the vibration amplitude of the rotating frequency, which is a typical feature of the inner-race failure [35]. Therefore, a failure in the inner-race of the bearing can be determined.

The FFT spectra of the serious inner-race faults are shown in Figs. 14(a) (0 to 50 Hz) and (b) (0 to 10 Hz). In the frequency range of 0 to 50 Hz, spectral peaks occur at the frequency of 6.2500 Hz and its harmonics (12.5313, 18.7813, 25.0625, 31.3438, 37.5938 and 44.6250 Hz). The frequency sidebands of 0.75 Hz are determined (as shown clearly in Fig. 14(b)) with decreasing amplitudes at both sides of these frequencies. Hence, a failure is determined in the inner-race of the bearing.

The FFT spectrum of the slight outer-race faults is shown in Fig. 15. In the frequency range of 0 to 50 Hz, spectral peaks occur at the frequency of 4.3750 Hz and its harmonics (8.7500, 13.1250, 17.4688, 21.8438, 26.2188, 30.5938, 34.9688, 39.3125, 43.6875 and 48.0625 Hz). Moreover, the frequency of 4.3750 Hz is close to the outer-race fault characteristic frequency of 4.3658 Hz calculated in Table 3. Discrete spectral peaks exist in the outer-race fault characteristic frequency and its harmonics, which is a typical feature of outer-race failure [35]. Therefore, a failure occurs in the outer-race of the bearing.

The FFT spectrum of the serious outer-race faults is shown in Fig. 16. In the frequency range of 0 to 50 Hz, spectral peaks exist at the frequency of 4.3125 Hz and its harmonics (8.6563, 12.9688, 17.2813, 21.6250, 25.9375, 30.2500, 34.5938, 38.9063, 43.2188 and 47.5313 Hz). Thus, a failure is also determined in the outer-race of the bearing.

The FFT spectra of the slight ball faults are shown in Figs. 17(a) (0 to 50 Hz) and (b) (0 to 10 Hz). In the frequency range of 0 to 50 Hz, spectral peaks are identified at the frequency of 2.1875 Hz and its harmonics (4.3750, 6.5625, 8.8750 and

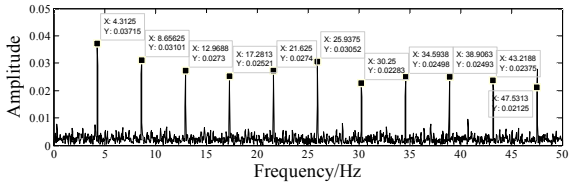

Fig. 16. FFT spectrum of serious outer-race fault signal (0 Hz to 50 Hz).

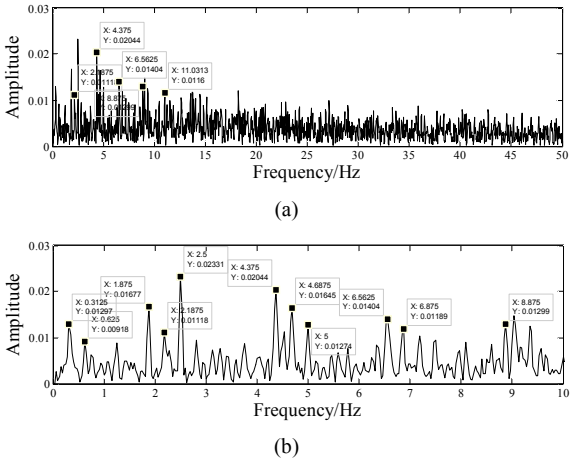

Fig. 17. FFT spectra of slight ball fault signal: (a) 0 to 50 Hz; (b) 0 to 10 Hz.

11.0313 Hz). The frequency sidebands of 0.312 Hz (as shown clearly in Fig. 17(b)) are also observed at one or both sides of some harmonics.

The frequency of 2.1875 Hz is close to the ball fault characteristic frequency of 2.1634 Hz calculated in Table 3, and the frequency of 0.3125Hz is close to the cage fault characteristic frequency of 0.3118 Hz. The vibration amplitude of the ball fault characteristic frequency is modulated by the vibration amplitude of the cage fault characteristic frequency, which is a typical feature of ball failure [35]. Therefore, a failure occurs in the ball of the bearing.

The FFT spectras of the serious ball faults are shown in Figs. 18(a) (0 to 50 Hz) and (b) (0 to 10 Hz). In the frequency range of 0 to 50 Hz, spectral peaks occur at the frequency of 2.2813 Hz and its harmonics (4.5625, 6.8438 and 9.1250 Hz), and frequency sidebands of 0.3125 Hz (as shown clearly in Fig. 18(b)) exist at one or both sides of some harmonics. Thus, a failure is determined in the ball of the bearing.

In summary, the FFT spectrum without correction can accurately indicate whether a fault occurs and the location of such a fault in the axle box bearings. However, can the amplitude of this method be used to judge the fault degree of bearings? To answer this question, we extract the amplitudes of the first visible four-order harmonics of six fault signals, as shown in Table 5.

Table 5 indicates that, for the outer-race and ball faults, all the amplitudes of slight faults (*S4*,*S6*) are smaller than those of serious faults (*S5*,*S7*). For the inner-race faults, except the

Table 5. Amplitudes of the fault characteristic frequency and its harmonics among six signals.

Amplitude / Running state	*f*	2*f*	3*f*	4*f*
S2	0.07037	0.05947	0.06439	0.06117
S3	0.06960	0.07520	0.05080	0.05100
S4	0.01439	0.01465	0.01140	0.01211
S5	0.03715	0.03101	0.02730	0.02521
S6	0.01118	0.02044	0.01404	0.01299
S7	0.03280	0.03630	0.02470	0.01640

* *f* denotes the fault frequency; 2*f*, 3*f* and 4*f* denote 2, 3 and 4 times the fault frequency, respectively.

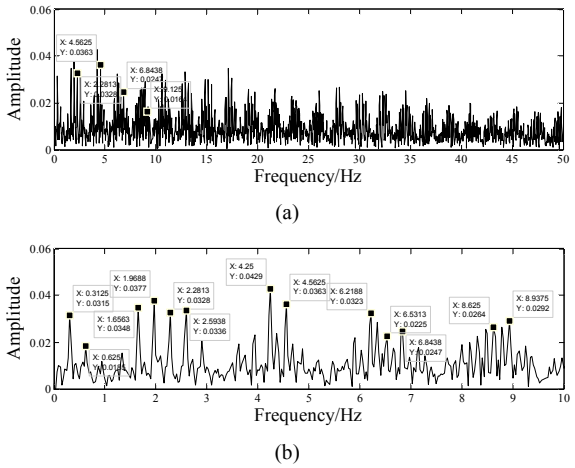

Fig. 18. FFT spectra of serious ball fault signal: (a) 0 Hz to 50 Hz; (b) 0 Hz to 10 Hz.

amplitude of the second-order harmonic of *S2* (0.05947) is smaller than that of *S3* (0.07520), the other harmonic amplitudes of *S2* are larger than those of *S3*. Therefore, the amplitudes of the FFT spectrum without correction cannot distinguish the fault degree of the bearings.

5.3 Quantitative diagnosis method based on the RPNWF

Apart from the 10 envelop signals of the normal state, the RPNWF spectrum analysis is performed on the other envelop signals obtained in Subsec. 5.2, after which 10 sets of data in each fault state are obtained.

We also feed the same samples into the interpolation correction (IPC) [30, 36], energy centrobaric correction (ECC) [37, 38], the PDC [26, 39], the RPDC and the RPBWF methods for the comparison of correction results. This was done in order t to clearly demonstrate the advantages of the RPNWF method in the fault diagnosis of axle box bearing compared with other methods. The peak detection interval of all methods is ±0.15 of the theoretical frequency of each order harmonic. The parameters of each order of harmonics are extracted, as shown in Table 6.

Table 6. Parameters of the first four harmonics among six fault signals.

Fault state	Calculation method	Parameter	Fault characteristic frequency and its harmonics			
			f	2*f*	3*f*	4*f*
S2	**Theoretical frequency**		**6.1342**	**12.2684**	**18.4026**	**24.5368**
	Without Correction	Frequency	6.2188	12.4688	18.6875	24.9063
		Amplitude	0.07037	0.05947	0.06439	0.06117
	IPC	Frequency	6.2169	12.4336	18.6501	24.8681
		Amplitude	0.07291	0.06018	0.06499	0.06251
	ECC	Frequency	6.2160	12.4349	18.6509	24.8672
		Amplitude	0.07340	0.06091	0.06447	0.06323
	PDC	Frequency	6.2171	12.4338	18.6596	24.8663
		Amplitude	0.07302	0.06057	0.06443	0.06322
	RPDC	Frequency	6.2183	12.4582	18.6747	24.8700
		Amplitude	0.07212	0.06240	0.06961	0.06490
	RPBWF	Frequency	6.2179	12.4343	18.6659	24.8690
		Amplitude	0.07366	0.06198	0.06489	0.06747
	RPNWF	Frequency	6.2171	12.4338	18.6596	24.8663
		Amplitude	0.07371	0.06320	0.06449	0.06271
S3	**Theoretical frequency**		**6.1342**	**12.2684**	**18.4026**	**24.5368**
	Without Correction	Frequency	6.2500	12.5313	18.7813	25.0625
		Amplitude	0.06960	0.07520	0.05080	0.05100
	IPC	Frequency	6.2450	12.4887	18.7342	24.9798
		Amplitude	0.07937	0.08378	0.06496	0.06419
	ECC	Frequency	6.2449	12.4814	18.7353	24.9879
		Amplitude	0.07967	0.08361	0.06289	0.06248
	PDC	Frequency	6.2454	12.4983	18.7345	24.9793
		Amplitude	0.07949	0.08592	0.06528	0.06495
	RPDC	Frequency	6.2496	12.5098	18.7434	25.0003
		Amplitude	0.07294	0.07719	0.07064	0.06717
	RPBWF	Frequency	6.2475	12.4984	18.7400	24.9961
		Amplitude	0.07799	0.07996	0.06903	0.06971
	RPNWF	Frequency	6.2454	12.4983	18.7345	24.9793
		Amplitude	0.08048	0.08076	0.06995	0.06954
S4	**Theoretical frequency**		**4.3658**	**8.7316**	**13.0974**	**17.4632**
	Without Correction	Frequency	4.3750	8.7500	13.1250	17.4688
		Amplitude	0.01439	0.01465	0.01140	0.01211
	IPC	Frequency	4.3743	8.7417	13.1203	17.4662
		Amplitude	0.01742	0.01810	0.01673	0.01644
	ECC	Frequency	4.3745	8.7419	13.1192	17.4674
		Amplitude	0.01733	0.01804	0.01668	0.01632
	PDC	Frequency	4.3731	8.7412	13.1228	17.4643
		Amplitude	0.01780	0.01785	0.01737	0.01716
	RPDC	Frequency	4.3740	8.7481	13.1248	17.4679
		Amplitude	0.01409	0.01416	0.01316	0.01140
	RPBWF	Frequency	4.3743	8.7426	13.1232	17.4654
		Amplitude	0.01602	0.01780	0.01657	0.01644
	RPNWF	Frequency	4.3731	8.7412	13.1228	17.4643
		Amplitude	0.01732	0.01804	0.01672	0.01655
S5	**Theoretical frequency**		**4.3658**	**8.7316**	**13.0974**	**17.4632**
	Without Correction	Frequency	4.3125	8.6563	12.9688	17.2813
		Amplitude	0.03715	0.03101	0.02730	0.02521
	IPC	Frequency	4.3293	8.6585	12.9916	17.3195
		Amplitude	0.03985	0.03697	0.03371	0.03360
	ECC	Frequency	4.3294	8.6589	12.9902	17.3193
		Amplitude	0.03971	0.03691	0.03401	0.03354
	PDC	Frequency	4.3303	8.6588	12.9932	17.3230
		Amplitude	0.04240	0.03695	0.03153	0.03043
	RPDC	Frequency	4.3291	8.6570	12.9824	17.3028
		Amplitude	0.03274	0.03604	0.0257	0.03080
	RPBWF	Frequency	4.3302	8.6574	12.9837	17.3036
		Amplitude	0.03916	0.03559	0.03398	0.03543
	RPNWF	Frequency	4.3303	8.6588	12.9932	17.3230
		Amplitude	0.04015	0.03690	0.03380	0.03442
S6	**Theoretical frequency**		**2.1634**	**4.3268**	**6.4902**	**8.6536**
	Without Correction	Frequency	2.1875	4.3750	6.5625	8.8750
		Amplitude	0.01118	0.02044	0.01404	0.01299
	IPC	Frequency	2.1730	4.3197	6.4628	8.7064
		Amplitude	0.01203	0.02673	0.02011	0.01702
	ECC	Frequency	2.1614	4.4701	6.4676	8.7020
		Amplitude	0.01451	0.02136	0.02074	0.01813
	PDC	Frequency	2.1610	4.3205	6.4333	8.7076
		Amplitude	0.02042	0.02688	0.01747	0.01882
	RPDC	Frequency	2.1772	4.3199	6.4295	8.7114
		Amplitude	0.01414	0.02503	0.02615	0.02707
	RPBWF	Frequency	2.1714	4.3168	6.4304	8.7078
		Amplitude	0.01761	0.02455	0.03000	0.0313
	RPNWF	Frequency	2.1610	4.3205	6.4333	8.7076
		Amplitude	0.01781	0.02674	0.01991	0.01716
S7	**Theoretical frequency**		**2.1634**	**4.3268**	**6.4902**	**8.6536**
	Without Correction	Frequency	2.2813	4.5625	6.8438	9.1250
		Amplitude	0.03280	0.03630	0.02470	0.01640
	IPC	Frequency	2.1599	4.3719	6.3675	8.7496
		Amplitude	0.03634	0.04097	0.04781	0.03207
	ECC	Frequency	2.1781	4.3763	6.3768	8.7576
		Amplitude	0.05649	0.04153	0.05165	0.03474
	PDC	Frequency	2.1772	4.3652	6.3837	8.7457
		Amplitude	0.05827	0.06901	0.02629	0.02494
	RPDC	Frequency	2.1854	4..3744	6.3783	8.7492
		Amplitude	0.03620	0.03609	0.02763	0.02740
	RPBWF	Frequency	2.1796	4.3694	6.3795	8.7466
		Amplitude	0.03831	0.03522	0.03428	0.03155
	RPNWF	Frequency	2.1772	4.3652	6.3837	8.7457
		Amplitude	0.03849	0.03740	0.04275	0.03053

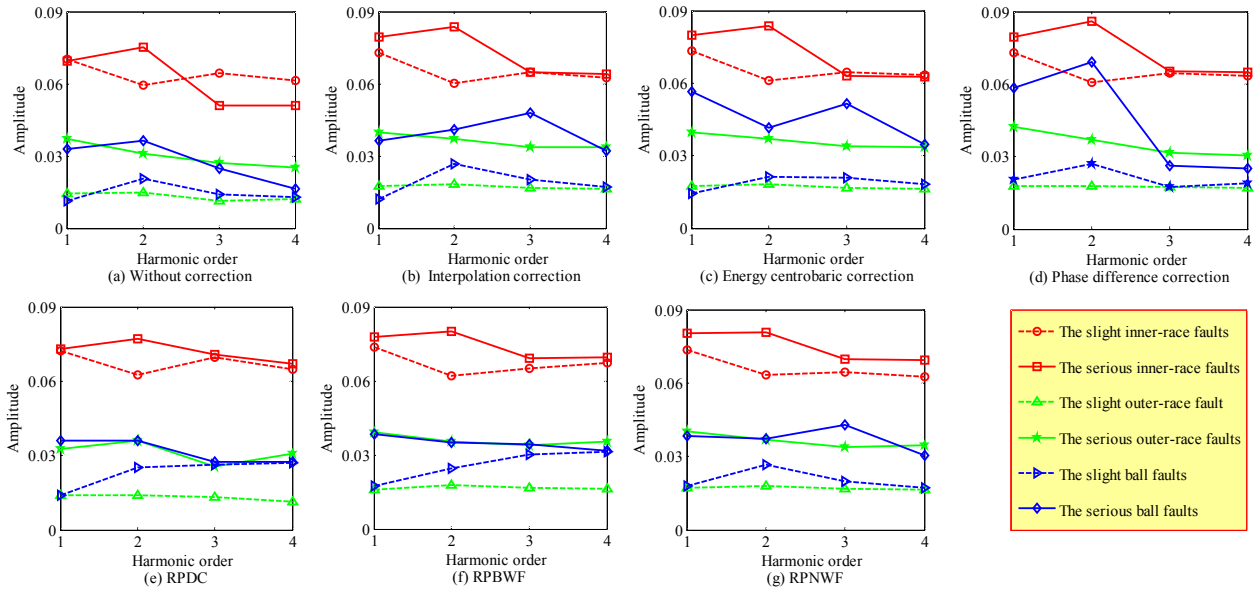

Fig. 19. Amplitudes of each fault state with various calculation methods: (a) Without correction; (b) IPC; (c) ECC; (d) PDC; (e) RPDC; (f) RPBWF; (g) RPNWF.

Table 6 indicates that, in each fault state, the frequencies calculated by all the seven methods (without correction and the IPC, ECC, PDC, RPDC, RPBWF and RPNWF) have minimal differences from the theoretical frequency. The theoretical frequency is calculated under the condition of constant speed and pure rolling of all balls, which are difficult to achieve in practice. The PDC and RPNWF adopt the phase difference method with the Nuttall43 window to correct the frequency; therefore, the frequencies calculated by the two methods are the same.

Table 6 also indicates that, in each fault state, the frequencies calculated by all the correction methods (the IPC, ECC, PDC, RPDC, RPBWF and RPNWF) are closer to the theoretical frequency than that of the method without correction. Most of the corrected amplitudes are higher than that of the uncorrected one, which proves that the six methods (the IPC, ECC, PDC, RPDC, RPBWF and RPNWF) are effective in preventing spectrum leakage.

Next, we plot the amplitudes versus the order of harmonic frequency from each fault state in Table 6 in Figs. 19(a)-(g). This was done in order to intuitively investigate whether the corrected amplitudes are effective in identifying the fault degree of the axle box bearings.

From Figs. 19(a)-(g), we can see that the amplitude curves of the outer-race faults are all smooth, and the amplitude difference among the same-order harmonics of all the methods is relatively small. On the contrary, each order amplitude curve of inner-race and ball faults fluctuates relatively significantly, and the corresponding amplitudes of some order harmonics are distinctly different, such as the second-order harmonic amplitude in the serious ball faults. Therefore, the above methods achieve good correction effects on sparse spectrum (outer-race faults) with frequency interval of each order that is far away and without side frequency interference. In comparison, the correction effect for the dense spectrum (inner-race and ball faults) with side frequency interference is relatively poor.

Theoretically, if the spectrum energy is not leaked or the correction method is effective, serious fault degree results in large harmonic amplitudes of the spectrum. From Fig. 19(g), we can see that significant amplitude differences exist in different fault states. Such differences are sufficient to distinguish the fault degree under the same fault location (serious faults > slight faults), indicating that the RPNWF method is effective for fault quantitative diagnosis. However, in Figs. 19(a)-(f), the fault degrees of outer-race faults (green curve) and ball faults (blue curve) can barely be separated (serious faults > slight faults), but the effectiveness of these methods in other two situations (inner-race and ball faults) is unsatisfactory.

In Fig. 19(a), in addition to the two points at abscissa 1 coinciding with each other, an obvious cross point exists between the two red curves at approximately abscissa 2.5. The third- and fourth-order harmonic amplitudes of the serious inner-race faults are obviously smaller than those of slight inner-race faults, which is inconsistent with the actual situation. This result proves that we cannot quantitatively diagnose the fault degrees of rolling bearing by discrete spectrum without correction.

Moreover, the third and fourth values of the two red curves in Figs. 19(b)-(d) yield close values, which makes it difficult to distinguish between the two states of slight and serious inner-race faults.

The curves with the same color in Fig. 19(e) have four potential coincidence points (both red and blue curves are two), which correspond to the first and third harmonic amplitudes of

the inner-race faults and the third and fourth harmonic amplitudes of the ball faults, respectively. In Fig. 19(f), the number of such coincidence points is only one, which corresponds to the fourth harmonic amplitudes of the ball faults. However, no such point is observed in Fig. 19(g). Thus, the RPDC method may be misjudged in the severity of inner-race and ball faults, and the effect of the amplitude correction is the worst among the three methods. The RPBWF method is also difficult to diagnose the ball faults quantitatively, and the effect of amplitude correction is located between the RPDC and RPNWF methods. The RPNWF method can distinguish the fault degrees in three different fault locations (outer-race, inner-race, and ball), and the amplitude correction effect is the best among the three methods. These results are consistent with those obtained in the simulation analysis.

The RPNWF method proposed in this study is effective in the quantitative fault diagnosis of the seven signals with different faults of axle box bearings used in this study. The amplitudes of the fault characteristic frequency and its harmonics extracted by this method can help obtain the axle box bearing's fault and the degree of such fault.

6. Conclusions

The following conclusions can be drawn based on the study's main findings:

a. For the seven signals with different fault locations and fault degrees of axle box bearings used in this study, the traditional FFT algorithm without correction can be used to identify whether the bearing is faulty and, if so, the location of such a fault; however, it cannot identify the fault degree.

b. For the seven signals with different fault locations and fault degrees of axle box bearings used in this study, the RPNWF can effectively distinguish the seven signals with different fault locations and fault degrees of the axle box bearings on UWL. Its amplitude correction effect is better than those of the traditional discrete spectrum correction methods, such as the IPC, ECC, PDC methods.

c. The fault setting experiments prove that the idea of integrating the fault diagnosis system of axle box bearings based on vibration monitoring with UWL is feasible and practically applicable.

In terms of its limitations, this study categorizes the states of the axle box bearings into only seven classes under the circumstance of small samples. Moreover, the faults are generated artificially, which may be different from the reality. Thus, realistic samples should be supplemented with various health states to test the capability of the proposed method confidently for multiple classifications.

Acknowledgments

This work was partly supported by the following: The Applied Basic Research Programs of Science and Technology Department of Sichuan Province (2018JY0238), the Major Project of Education Department in Sichuan Province (17ZA0354), the National Natural Science Foundation of China (51775448), the Project of Spring Plan of the Ministry of Education (Z2012024), the Science and Technology Research and Development Program of Sichuan Province (2017GZ0103), the Open Research Subject of Key Laboratory of Fluid and Power Machinery (Xihua University), the Ministry of Education (szjj2016-013), the Key Scientific Research Fund Project of Xihua University (z1620303), and the Open Research Subject of the Key Laboratory of Automotive Measurement, Control, and Safety (Xihua University) (szjj2017-078).

References

[1] Y. F. Li et al., Train axle bearing fault detection using a feature selection scheme based multi-scale morphological filter, *Mechanical Systems and Signal Processing*, 101 (2018) 435-448.

[2] Q. Xiao et al., Analysis of the wheel/rail rolling contact fatigue of a high-speed train under the transient mechanism, *Journal of Mechanical Science & Technology*, 31 (5) (2017) 2235-2242.

[3] K. Zhang et al., Research on eddy current pulsed thermography for rolling contact fatigue crack detection and quantification in wheel tread, *2016 18th International Wheelset Congress (IWC)* (2017) 5-11.

[4] X. W. Wu and M. R. Chi, Study on stress states of a wheelset axle due to a defective wheel, *Journal of Mechanical Science & Technology*, 30 (11) (2016) 4845-4857.

[5] C. Klinger and D. Bettge, Axle fracture of an ICE3 high speed train, *Engineering Failure Analysis*, 35 (2013) 66-81.

[6] Q. Xiong, Research on feature extraction and fault diagnosis method of vibration signal of rolling bearing in train, *Ph.D. Thesis,* Southwest Jiaotong University, Chengdu, China (2015).

[7] A. Amini et al., Wayside detection of faults in railway axle bearings using time spectral kurtosis analysis on high frequency acoustic emission signals, *Advances in Mechanical Engineering*, 8 (11) (2016) 1-9.

[8] T. Nijssen and H. J. Reiche, Underfloor wheel set lathe for machining wheel sets of railway vehicles, *European Patent*, EP1836018 (2007).

[9] A. R. Andrade and J. Stow, Assessing the efficiency of maintenance operators: A case study of turning railway wheelsets on an under-floor wheel lathe, *Proceedings of the Institution of Mechanical Engineers, Part O: Journal of Risk and Reliability*, 231 (2) (2017) 155-163.

[10] C. Vale et al., Novel efficient technologies in Europe for axle bearing condition monitoring-the MAXBE project, *Transportation Research Procedia*, 14 (2016) 635-644.

[11] A. Amini et al., Onboard detection of railway axle bearing defects using envelope analysis of high frequency acoustic emission signals, *Case Studies in Nondestructive Testing &*

Evaluation, 6 (2016) 8-16.

[12] H. Zhang et al., Multi-bearing defect detection with track-side acoustic signal based on a pseudo time- frequency analysis and Dopplerlet filter, *Mechanical Systems & Signal Processing*, s70-71 (4) (2016) 176-200.

[13] M. Asplund et al., Condition monitoring and e-maintenance solution of railway wheels, *Journal of Quality in Maintenance Engineering*, 20 (3) (2014) 216-232.

[14] J. J. Zhang and Q. F. Zhang, The underfloor wheelset replacement device of axle box bearing in Shaoshan locomotives, *Electric Drive for Locomotives*, 6 (2011) 83-84.

[15] V. C. Tao et al., Processing method of locomotive wheel wear statistical data and predication model of turning period, *Journal of the China Railway Society*, 37 (12) (2015) 14-19.

[16] H. J. Sun, Discussion on bearing service life of passenger electric locomotives, *Railway Locomotive & Car*, 30 (6) (2010) 88-90.

[17] H. B. Wei, The analysis and treatment of common faults of U2000-400 type underfloor wheelset lathe, *Shanghai Railway Science & Technology*, 2 (2016) 123-125.

[18] J. M. Yan and M. H. Fu, *Vehicle engineering,* 3rd ed, Beijing, China: China Railway Publishing Press (2009) 43-46.

[19] N. Wang et al., Study on fault diagnosis of low-speed rolling bearing using stress waves and wavelet analysis, *Journal of Vibration Engineering*, 20 (3) (2007) 280-284.

[20] J. Schoukens, Y. Rolain and R. Pintelon, Analysis of windowing/leakage effects in frequency response function measurements, *Automatica*., 42 (1) (2006) 27-38.

[21] K. Ding, M. Xie and X. F. Zhang, Phase difference correction method for phase and frequency in spectral analysis, *Mechanical Systems and Signal Processing*, 14 (5) (2000) 835-843.

[22] W. B. Hu et al., An improved frequency spectrum correction method based on phase difference correction method, *Journal of Vibration and Shock*, 31 (1) (2012) 162-166.

[23] A. H. Nuttall, Some windows with very good sidelobe behavior, *IEEE Transactions on Acoustics Speech & Signal Processing*, 29 (1) (1981) 84-91.

[24] X. Y. Qiu and F. L. Li, Microgrid harmonic detection algorithm based on Nuttall window DFT correction, *Journal of Electric Power Science And Technology*, 32 (1) (2017) 65-70.

[25] Y. Xiao et al., Fast Quasi-synchronous harmonic algorithm based on weight window function - mixed radix FFT, *2016 IEEE International Workshop on Applied Measurements for Power Systems (AMPS)* (2016).

[26] B. Zeng et al., Harmonic phasor analysis based on improved FFT algorithm, *IEEE Transactions on Smart Grid*, 2 (1) (2011) 51-59.

[27] L. G. Cai, G. H. Sun and Z. F. Liu, The dynamic characteristic and finite element analysis on wheelset driving system of underfloor wheelset lathe, *2014 International Conference on Mechanics and Civil Engineering (ICMCE-14)* (2014) 292-298.

[28] P. Wang and M. F. Liao, Adaptive demodulated resonance technique for the rolling bearing fault diagnosis, *Journal of Aerospace Power*, 20 (4) (2005) 606-612.

[29] F. J. Harris, On the use of harmonic analysis with the discrete Fourier transform, *Proceedings of the IEEE*, 66 (1) (1978) 51-83.

[30] T. Grandke, Interpolation algorithms for discrete fourier transforms of weighted signals, *IEEE Transactions on Instrumentation & Measurement*, 32 (2) (1983) 350-355.

[31] X. Y. He et al., Fault diagnosis of rolling bearing based on acceleration envelope technique, *China Plant Engineering*, 10 (2017) 63-65.

[32] Y. T. Sheen, On the study of applying morlet wavelet to the Hilbert transform for the envelope detection of bearing vibrations, *Mechanical Systems and Signal Processing,* 23 (5) (2009) 1518-1527.

[33] M. Unser, A. Aldroubi and M. Eden, Polynomial spline signal approximations: filter design and asymptotic equivalence with Shannon's sampling theorem, *IEEE Transactions on Information Theory*, 38 (1) (1992) 95-103.

[34] H. Jiang, Y. Xia and X. Wang, Rolling bearing fault detection using an adaptive lifting multiwavelet packet with a $1\frac{1}{2}$ dimension spectrum, *Measurement Science & Technology*, 24 (12) (2013) 125002-125011.

[35] N. Tandon and A. Choudhury, An analytical model for the prediction of the vibration response of rolling element bearings due to a localized defect, *Journal of Sound and Vibration,* 205 (3) (1997) 275-292.

[36] K. Ding, M. Xie and Z. J. Yang, *The theory and technology of discrete spectrum correction*, Beijing, China: Science Press (2009) 101-110.

[37] X. He et al., Spatial filtering velocimeter using frequency shifting by the method of rotating kernel, *Measurement*, 73 (2015) 15-23.

[38] K. Ding and L. Q. Jiang, Energy centrobaric correction method for discrete spectrum, *Journal of Vibration Engineering*, 14 (3) (2001) 354-358.

[39] J. Luo and M. Xie, Phase difference methods based on asymmetric windows, *Mechanical Systems & Signal Processing*, 54-55 (2015) 52-67.

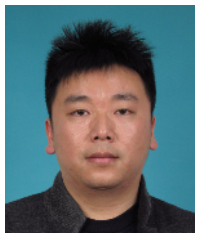

Qing Xiong received his Ph.D. from Southwest Jiaotong University, China in 2015. He is currently a lecturer at the School of Automobile and Transportation, Xihua University, China. His current research interests are the fault diagnosis of mechanical systems using numerical simulation and signal-processing techniques.